

Cross section measurements of the $e^+e^- \rightarrow D^{*+}D^{*-}$ and $e^+e^- \rightarrow D^{*+}D^-$ processes at center-of-mass energies from 4.085 to 4.600 GeV

The BESIII Collaboration



M. Ablikim¹, M. N. Achasov^{10,b}, P. Adlarson⁶⁸, M. Albrecht⁴, R. Aliberti²⁸, A. Amoroso^{67A,67C}, M. R. An³², Q. An^{64,50}, X. H. Bai⁵⁸, Y. Bai⁴⁹, O. Bakina²⁹, R. Baldini Ferroli^{23A}, I. Balossino^{24A}, Y. Ban^{39,h}, V. Batozskaya^{1,37}, D. Becker²⁸, K. Begzsuren²⁶, N. Berger²⁸, M. Bertani^{23A}, D. Bettoni^{24A}, F. Bianchi^{67A,67C}, J. Bloms⁶¹, A. Bortone^{67A,67C}, I. Boyko²⁹, R. A. Briere⁵, A. Brueggemann⁶¹, H. Cai⁶⁹, X. Cai^{1,50}, A. Calcaterra^{23A}, G. F. Cao^{1,55}, N. Cao^{1,55}, S. A. Cetin^{54A}, J. F. Chang^{1,50}, W. L. Chang^{1,55}, G. Chelkov^{29,a}, C. Chen³⁶, G. Chen¹, H. S. Chen^{1,55}, M. L. Chen^{1,50}, S. J. Chen³⁵, T. Chen¹, X. R. Chen^{25,55}, X. T. Chen¹, Y. B. Chen^{1,50}, Z. J. Chen^{20,i}, W. S. Cheng^{67C}, X. Chu³⁶, G. Cibinetto^{24A}, F. Cossio^{67C}, J. J. Cui⁴², H. L. Dai^{1,50}, J. P. Dai⁷¹, A. Dbeysi¹⁴, R. E. de Boer⁴, D. Dedovich²⁹, Z. Y. Deng¹, A. Denig²⁸, I. Denysenko²⁹, M. Destefanis^{67A,67C}, F. De Mori^{67A,67C}, Y. Ding³³, J. Dong^{1,50}, L. Y. Dong^{1,55}, M. Y. Dong^{1,50,55}, X. Dong⁶⁹, S. X. Du⁷³, P. Egorov^{29,a}, Y. L. Fan⁶⁹, J. Fang^{1,50}, S. S. Fang^{1,55}, W. X. Fang¹, Y. Fang¹, R. Farinelli^{24A}, L. Fava^{67B,67C}, F. Feldbauer⁴, G. Felici^{23A}, C. Q. Feng^{64,50}, J. H. Feng⁵¹, K. Fischer⁶², M. Fritsch⁴, C. F. Fritzsch⁶¹, C. D. Fu¹, H. Gao⁵⁵, Y. N. Gao^{39,h}, Yang Gao^{64,50}, S. Garbolino^{67C}, I. Garzia^{24A,24B}, P. T. Ge⁶⁹, C. Geng⁵¹, E. M. Gersabeck⁵⁹, A. Gilman⁶², K. Goetzen¹¹, L. Gong³³, W. X. Gong^{1,50}, W. Gradl²⁸, M. Greco^{67A,67C}, M. H. Gu^{1,50}, C. Y. Guan^{1,55}, A. Q. Guo^{25,55}, L. B. Guo³⁴, R. P. Guo⁴¹, Y. P. Guo^{9,g}, A. Guskov^{29,a}, T. T. Han⁴², W. Y. Han³², X. Q. Hao¹⁵, F. A. Harris⁵⁷, K. K. He⁴⁷, K. L. He^{1,55}, F. H. Heinsius⁴, C. H. Heinz²⁸, Y. K. Heng^{1,50,55}, C. Herold⁵², M. Himmelreich^{11,e}, T. Holtmann⁴, G. Y. Hou^{1,55}, Y. R. Hou⁵⁵, Z. L. Hou¹, H. M. Hu^{1,55}, J. F. Hu^{48,j}, T. Hu^{1,50,55}, Y. Hu¹, G. S. Huang^{64,50}, K. X. Huang⁵¹, L. Q. Huang⁶⁵, L. Q. Huang^{25,55}, X. T. Huang⁴², Y. P. Huang¹, Z. Huang^{39,h}, T. Hussain⁶⁶, N. Hüsken^{22,28}, W. Imoehl²², M. Irshad^{64,50}, J. Jackson²², S. Jaeger⁴, S. Janchiv²⁶, Q. Ji¹, Q. P. Ji¹⁵, X. B. Ji^{1,55}, X. L. Ji^{1,50}, Y. Y. Ji⁴², Z. K. Jia^{64,50}, H. B. Jiang⁴², S. S. Jiang³², X. S. Jiang^{1,50,55}, Y. Jiang⁵⁵, J. B. Jiao⁴², Z. Jiao¹⁸, S. Jin³⁵, Y. Jin⁵⁸, M. Q. Jing^{1,55}, T. Johansson⁶⁸, N. Kalantar-Nayestanaki⁵⁶, X. S. Kang³³, R. Kappert⁵⁶,

M. Kavatsyuk⁵⁶, B. C. Ke⁷³, I. K. Keshk⁴, A. Khoukaz⁶¹, P. Kiese²⁸, R. Kiuchi¹, R. Kliemt¹¹, L. Koch³⁰, O. B. Kolcu^{54A}, B. Kopf⁴, M. Kuemmel⁴, M. Kuessner⁴, A. Kupsc^{37,68}, W. Kühn³⁰, J. J. Lane⁵⁹, J. S. Lange³⁰, P. Larin¹⁴, A. Lavania²¹, L. Lavezzi^{67A,67C}, Z. H. Lei^{64,50}, H. Leithoff²⁸, M. Lellmann²⁸, T. Lenz²⁸, C. Li³⁶, C. Li⁴⁰, C. H. Li³², Cheng Li^{64,50}, D. M. Li⁷³, F. Li^{1,50}, G. Li¹, H. Li⁴⁴, H. Li^{64,50}, H. B. Li^{1,55}, H. J. Li¹⁵, H. N. Li^{48,j}, J. Q. Li⁴, J. S. Li⁵¹, J. W. Li⁴², Ke Li¹, L. J Li¹, L. K. Li¹, Lei Li³, M. H. Li³⁶, P. R. Li^{31,k,l}, S. X. Li⁹, S. Y. Li⁵³, T. Li⁴², W. D. Li^{1,55}, W. G. Li¹, X. H. Li^{64,50}, X. L. Li⁴², Xiaoyu Li^{1,55}, Z. Y. Li⁵¹, H. Liang^{1,55}, H. Liang^{64,50}, H. Liang²⁷, Y. F. Liang⁴⁶, Y. T. Liang^{25,55}, G. R. Liao¹², L. Z. Liao⁴², J. Libby²¹, A. Limphirat⁵², C. X. Lin⁵¹, D. X. Lin^{25,55}, T. Lin¹, B. J. Liu¹, C. X. Liu¹, D. Liu^{14,64}, F. H. Liu⁴⁵, Fang Liu¹, Feng Liu⁶, G. M. Liu^{48,j}, H. Liu^{31,k,l}, H. M. Liu^{1,55}, Huanhuan Liu¹, Huihui Liu¹⁶, J. B. Liu^{64,50}, J. L. Liu⁶⁵, J. Y. Liu^{1,55}, K. Liu¹, K. Y. Liu³³, Ke Liu¹⁷, L. Liu^{64,50}, M. H. Liu^{9,g}, P. L. Liu¹, Q. Liu⁵⁵, S. B. Liu^{64,50}, T. Liu^{9,g}, W. K. Liu³⁶, W. M. Liu^{64,50}, X. Liu^{31,k,l}, Y. Liu^{31,k,l}, Y. B. Liu³⁶, Z. A. Liu^{1,50,55}, Z. Q. Liu⁴², X. C. Lou^{1,50,55}, F. X. Lu⁵¹, H. J. Lu¹⁸, J. G. Lu^{1,50}, X. L. Lu¹, Y. Lu¹, Y. P. Lu^{1,50}, Z. H. Lu¹, C. L. Luo³⁴, M. X. Luo⁷², T. Luo^{9,g}, X. L. Luo^{1,50}, X. R. Lyu⁵⁵, Y. F. Lyu³⁶, F. C. Ma³³, H. L. Ma¹, L. L. Ma⁴², M. M. Ma^{1,55}, Q. M. Ma¹, R. Q. Ma^{1,55}, R. T. Ma⁵⁵, X. Y. Ma^{1,50}, Y. Ma^{39,h}, F. E. Maas¹⁴, M. Maggiora^{67A,67C}, S. Maldaner⁴, S. Malde⁶², Q. A. Malik⁶⁶, A. Mangoni^{23B}, Y. J. Mao^{39,h}, Z. P. Mao¹, S. Marcello^{67A,67C}, Z. X. Meng⁵⁸, J. G. Messchendorp^{56,d}, G. Mezzadri^{24A}, H. Miao¹, T. J. Min³⁵, R. E. Mitchell²², X. H. Mo^{1,50,55}, N. Yu. Muchnoi^{10,b}, H. Muramatsu⁶⁰, Y. Nefedov²⁹, F. Nerling^{11,e}, I. B. Nikolaev^{10,b}, Z. Ning^{1,50}, S. Nisar^{8,m}, Y. Niu⁴², S. L. Olsen⁵⁵, Q. Ouyang^{1,50,55}, S. Pacetti^{23B,23C}, X. Pan^{9,g}, Y. Pan⁵⁹, A. Pathak¹, A. Pathak²⁷, M. Pelizaeus⁴, H. P. Peng^{64,50}, K. Peters^{11,e}, J. Pettersson⁶⁸, J. L. Ping³⁴, R. G. Ping^{1,55}, S. Plura²⁸, S. Pogodin²⁹, R. Poling⁶⁰, V. Prasad^{64,50}, F. Z. Qi¹, H. Qi^{64,50}, H. R. Qi⁵³, M. Qi³⁵, T. Y. Qi^{9,g}, S. Qian^{1,50}, W. B. Qian⁵⁵, Z. Qian⁵¹, C. F. Qiao⁵⁵, J. J. Qin⁶⁵, L. Q. Qin¹², X. P. Qin^{9,g}, X. S. Qin⁴², Z. H. Qin^{1,50}, J. F. Qiu¹, S. Q. Qu⁵³, S. Q. Qu³⁶, K. H. Rashid⁶⁶, C. F. Redmer²⁸, K. J. Ren³², A. Rivetti^{67C}, V. Rodin⁵⁶, M. Rolo^{67C}, G. Rong^{1,55}, Ch. Rosner¹⁴, S. N. Ruan³⁶, H. S. Sang⁶⁴, A. Sarantsev^{29,c}, Y. Schelhaas²⁸, C. Schnier⁴, K. Schoenning⁶⁸, M. Scodeggio^{24A,24B}, K. Y. Shan^{9,g}, W. Shan¹⁹, X. Y. Shan^{64,50}, J. F. Shangguan⁴⁷, L. G. Shao^{1,55}, M. Shao^{64,50}, C. P. Shen^{9,g}, H. F. Shen^{1,55}, X. Y. Shen^{1,55}, B.-A. Shi⁵⁵, H. C. Shi^{64,50}, J. Y. Shi¹, R. S. Shi^{1,55}, X. Shi^{1,50}, X. D Shi^{64,50}, J. J. Song¹⁵, W. M. Song^{27,1}, Y. X. Song^{39,h}, S. Sosio^{67A,67C}, S. Spataro^{67A,67C}, F. Stieler²⁸, K. X. Su⁶⁹, P. P. Su⁴⁷, Y.-J. Su⁵⁵, G. X. Sun¹, H. Sun⁵⁵, H. K. Sun¹, J. F. Sun¹⁵, L. Sun⁶⁹, S. S. Sun^{1,55}, T. Sun^{1,55}, W. Y. Sun²⁷, X Sun^{20,i}, Y. J. Sun^{64,50}, Y. Z. Sun¹, Z. T. Sun⁴², Y. H. Tan⁶⁹, Y. X. Tan^{64,50}, C. J. Tang⁴⁶, G. Y. Tang¹, J. Tang⁵¹, L. Y Tao⁶⁵, Q. T. Tao^{20,i}, J. X. Teng^{64,50}, V. Thoren⁶⁸, W. H. Tian⁴⁴, Y. Tian^{25,55}, I. Uman^{54B}, B. Wang¹, B. L. Wang⁵⁵, D. Y. Wang^{39,h}, F. Wang⁶⁵, H. J. Wang^{31,k,l}, H. P. Wang^{1,55}, K. Wang^{1,50}, L. L. Wang¹, M. Wang⁴², M. Z. Wang^{39,h}, Meng Wang^{1,55}, S. Wang^{9,g}, T. Wang^{9,g}, T. J. Wang³⁶, W. Wang⁵¹, W. H. Wang⁶⁹, W. P. Wang^{64,50}, X. Wang^{39,h}, X. F. Wang^{31,k,l}, X. L. Wang^{9,g}, Y. D. Wang³⁸, Y. F. Wang^{1,50,55},

Y. H. Wang⁴⁰, Y. Q. Wang¹, Ying Wang⁵¹, Z. Wang^{1,50}, Z. Y. Wang^{1,55},
Ziyi Wang⁵⁵, D. H. Wei¹², F. Weidner⁶¹, S. P. Wen¹, D. J. White⁵⁹, U. Wiedner⁴,
G. Wilkinson⁶², M. Wolke⁶⁸, L. Wollenberg⁴, J. F. Wu^{1,55}, L. H. Wu¹, L. J. Wu^{1,55},
X. Wu^{9,g}, X. H. Wu²⁷, Y. Wu⁶⁴, Z. Wu^{1,50}, L. Xia^{64,50}, T. Xiang^{39,h}, D. Xiao^{31,k,l},
H. Xiao^{9,g}, S. Y. Xiao¹, Y. L. Xiao^{9,g}, Z. J. Xiao³⁴, X. H. Xie^{39,h}, Y. Xie⁴²,
Y. G. Xie^{1,50}, Y. H. Xie⁶, Z. P. Xie^{64,50}, T. Y. Xing^{1,55}, C. F. Xu¹, C. J. Xu⁵¹,
G. F. Xu¹, Q. J. Xu¹³, S. Y. Xu⁶³, X. P. Xu⁴⁷, Y. C. Xu⁵⁵, F. Yan^{9,g}, L. Yan^{9,g},
W. B. Yan^{64,50}, W. C. Yan⁷³, H. J. Yang^{43,f}, H. L. Yang²⁷, H. X. Yang¹, L. Yang⁴⁴,
S. L. Yang⁵⁵, Tao Yang¹, Y. X. Yang^{1,55}, Yifan Yang^{1,55}, M. Ye^{1,50}, M. H. Ye⁷,
J. H. Yin¹, Z. Y. You⁵¹, B. X. Yu^{1,50,55}, C. X. Yu³⁶, G. Yu^{1,55}, T. Yu⁶⁵, C. Z. Yuan^{1,55},
L. Yuan², S. C. Yuan¹, X. Q. Yuan¹, Y. Yuan^{1,55}, Z. Y. Yuan⁵¹, C. X. Yue³²,
A. A. Zafar⁶⁶, F. R. Zeng⁴², X. Zeng Zeng⁶, Y. Zeng^{20,i}, Y. H. Zhan⁵¹, A. Q. Zhang¹,
B. L. Zhang¹, B. X. Zhang¹, D. H. Zhang³⁶, G. Y. Zhang¹⁵, H. Zhang⁶⁴,
H. H. Zhang⁵¹, H. H. Zhang²⁷, H. Y. Zhang^{1,50}, J. L. Zhang⁷⁰, J. Q. Zhang³⁴,
J. W. Zhang^{1,50,55}, J. X. Zhang^{31,k,l}, J. Y. Zhang¹, J. Z. Zhang^{1,55}, Jianyu Zhang^{1,55},
Jiawei Zhang^{1,55}, L. M. Zhang⁵³, L. Q. Zhang⁵¹, Lei Zhang³⁵, P. Zhang¹,
Q. Y. Zhang^{32,73}, Shulei Zhang^{20,i}, X. D. Zhang³⁸, X. M. Zhang¹, X. Y. Zhang⁴²,
X. Y. Zhang⁴⁷, Y. Zhang⁶², Y. T. Zhang⁷³, Y. H. Zhang^{1,50}, Yan Zhang^{64,50},
Yao Zhang¹, Z. H. Zhang¹, Z. Y. Zhang³⁶, Z. Y. Zhang⁶⁹, G. Zhao¹, J. Zhao³²,
J. Y. Zhao^{1,55}, J. Z. Zhao^{1,50}, Lei Zhao^{64,50}, Ling Zhao¹, M. G. Zhao³⁶, Q. Zhao¹,
S. J. Zhao⁷³, Y. B. Zhao^{1,50}, Y. X. Zhao^{25,55}, Z. G. Zhao^{64,50}, A. Zhemchugov^{29,a},
B. Zheng⁶⁵, J. P. Zheng^{1,50}, Y. H. Zheng⁵⁵, B. Zhong³⁴, C. Zhong⁶⁵, X. Zhong⁵¹, H.
Zhou⁴², L. P. Zhou^{1,55}, X. Zhou⁶⁹, X. K. Zhou⁵⁵, X. R. Zhou^{64,50}, X. Y. Zhou³²,
Y. Z. Zhou^{9,g}, J. Zhu³⁶, K. Zhu¹, K. J. Zhu^{1,50,55}, L. X. Zhu⁵⁵, S. H. Zhu⁶³,
T. J. Zhu⁷⁰, W. J. Zhu^{9,g}, Y. C. Zhu^{64,50}, Z. A. Zhu^{1,55}, B. S. Zou¹, J. H. Zou¹

¹ Institute of High Energy Physics, Beijing 100049, People's Republic of China

² Beihang University, Beijing 100191, People's Republic of China

³ Beijing Institute of Petrochemical Technology, Beijing 102617, People's Republic of China

⁴ Bochum Ruhr-University, D-44780 Bochum, Germany

⁵ Carnegie Mellon University, Pittsburgh, Pennsylvania 15213, USA

⁶ Central China Normal University, Wuhan 430079, People's Republic of China

⁷ China Center of Advanced Science and Technology, Beijing 100190, People's Republic of China

⁸ COMSATS University Islamabad, Lahore Campus, Defence Road, Off Raiwind Road, 54000 Lahore, Pakistan

⁹ Fudan University, Shanghai 200433, People's Republic of China

¹⁰ G.I. Budker Institute of Nuclear Physics SB RAS (BINP), Novosibirsk 630090, Russia

¹¹ GSI Helmholtzcentre for Heavy Ion Research GmbH, D-64291 Darmstadt, Germany

¹² Guangxi Normal University, Guilin 541004, People's Republic of China

¹³ Hangzhou Normal University, Hangzhou 310036, People's Republic of China

¹⁴ Helmholtz Institute Mainz, Staudinger Weg 18, D-55099 Mainz, Germany

- ¹⁵ Henan Normal University, Xinxiang 453007, People's Republic of China
¹⁶ Henan University of Science and Technology, Luoyang 471003, People's Republic of China
¹⁷ Henan University of Technology, Zhengzhou 450001, People's Republic of China
¹⁸ Huangshan College, Huangshan 245000, People's Republic of China
¹⁹ Hunan Normal University, Changsha 410081, People's Republic of China
²⁰ Hunan University, Changsha 410082, People's Republic of China
²¹ Indian Institute of Technology Madras, Chennai 600036, India
²² Indiana University, Bloomington, Indiana 47405, USA
²³ INFN Laboratori Nazionali di Frascati , (A)INFN Laboratori Nazionali di Frascati, I-00044, Frascati, Italy; (B)INFN Sezione di Perugia, I-06100, Perugia, Italy; (C)University of Perugia, I-06100, Perugia, Italy
²⁴ INFN Sezione di Ferrara, (A)INFN Sezione di Ferrara, I-44122, Ferrara, Italy; (B)University of Ferrara, I-44122, Ferrara, Italy
²⁵ Institute of Modern Physics, Lanzhou 730000, People's Republic of China
²⁶ Institute of Physics and Technology, Peace Ave. 54B, Ulaanbaatar 13330, Mongolia
²⁷ Jilin University, Changchun 130012, People's Republic of China
²⁸ Johannes Gutenberg University of Mainz, Johann-Joachim-Becher-Weg 45, D-55099 Mainz, Germany
²⁹ Joint Institute for Nuclear Research, 141980 Dubna, Moscow region, Russia
³⁰ Justus-Liebig-Universitaet Giessen, II. Physikalisches Institut, Heinrich-Buff-Ring 16, D-35392 Giessen, Germany
³¹ Lanzhou University, Lanzhou 730000, People's Republic of China
³² Liaoning Normal University, Dalian 116029, People's Republic of China
³³ Liaoning University, Shenyang 110036, People's Republic of China
³⁴ Nanjing Normal University, Nanjing 210023, People's Republic of China
³⁵ Nanjing University, Nanjing 210093, People's Republic of China
³⁶ Nankai University, Tianjin 300071, People's Republic of China
³⁷ National Centre for Nuclear Research, Warsaw 02-093, Poland
³⁸ North China Electric Power University, Beijing 102206, People's Republic of China
³⁹ Peking University, Beijing 100871, People's Republic of China
⁴⁰ Qufu Normal University, Qufu 273165, People's Republic of China
⁴¹ Shandong Normal University, Jinan 250014, People's Republic of China
⁴² Shandong University, Jinan 250100, People's Republic of China
⁴³ Shanghai Jiao Tong University, Shanghai 200240, People's Republic of China
⁴⁴ Shanxi Normal University, Linfen 041004, People's Republic of China
⁴⁵ Shanxi University, Taiyuan 030006, People's Republic of China
⁴⁶ Sichuan University, Chengdu 610064, People's Republic of China
⁴⁷ Soochow University, Suzhou 215006, People's Republic of China
⁴⁸ South China Normal University, Guangzhou 510006, People's Republic of China
⁴⁹ Southeast University, Nanjing 211100, People's Republic of China
⁵⁰ State Key Laboratory of Particle Detection and Electronics, Beijing 100049, Hefei 230026, People's Republic of China

- ⁵¹ Sun Yat-Sen University, Guangzhou 510275, People's Republic of China
⁵² Suranaree University of Technology, University Avenue 111, Nakhon Ratchasima 30000, Thailand
⁵³ Tsinghua University, Beijing 100084, People's Republic of China
⁵⁴ Turkish Accelerator Center Particle Factory Group, (A)Istinye University, 34010, Istanbul, Turkey; (B)Near East University, Nicosia, North Cyprus, Mersin 10, Turkey
⁵⁵ University of Chinese Academy of Sciences, Beijing 100049, People's Republic of China
⁵⁶ University of Groningen, NL-9747 AA Groningen, The Netherlands
⁵⁷ University of Hawaii, Honolulu, Hawaii 96822, USA
⁵⁸ University of Jinan, Jinan 250022, People's Republic of China
⁵⁹ University of Manchester, Oxford Road, Manchester, M13 9PL, United Kingdom
⁶⁰ University of Minnesota, Minneapolis, Minnesota 55455, USA
⁶¹ University of Muenster, Wilhelm-Klemm-Str. 9, 48149 Muenster, Germany
⁶² University of Oxford, Keble Rd, Oxford, UK OX13RH
⁶³ University of Science and Technology Liaoning, Anshan 114051, People's Republic of China
⁶⁴ University of Science and Technology of China, Hefei 230026, People's Republic of China
⁶⁵ University of South China, Hengyang 421001, People's Republic of China
⁶⁶ University of the Punjab, Lahore-54590, Pakistan
⁶⁷ University of Turin and INFN, (A)University of Turin, I-10125, Turin, Italy; (B)University of Eastern Piedmont, I-15121, Alessandria, Italy; (C)INFN, I-10125, Turin, Italy
⁶⁸ Uppsala University, Box 516, SE-75120 Uppsala, Sweden
⁶⁹ Wuhan University, Wuhan 430072, People's Republic of China
⁷⁰ Xinyang Normal University, Xinyang 464000, People's Republic of China
⁷¹ Yunnan University, Kunming 650500, People's Republic of China
⁷² Zhejiang University, Hangzhou 310027, People's Republic of China
⁷³ Zhengzhou University, Zhengzhou 450001, People's Republic of China
^a Also at the Moscow Institute of Physics and Technology, Moscow 141700, Russia
^b Also at the Novosibirsk State University, Novosibirsk, 630090, Russia
^c Also at the NRC "Kurchatov Institute", PNPI, 188300, Gatchina, Russia
^d Currently at Istanbul Arel University, 34295 Istanbul, Turkey
^e Also at Goethe University Frankfurt, 60323 Frankfurt am Main, Germany
^f Also at Key Laboratory for Particle Physics, Astrophysics and Cosmology, Ministry of Education; Shanghai Key Laboratory for Particle Physics and Cosmology; Institute of Nuclear and Particle Physics, Shanghai 200240, People's Republic of China
^g Also at Key Laboratory of Nuclear Physics and Ion-beam Application (MOE) and Institute of Modern Physics, Fudan University, Shanghai 200443, People's Republic of China
^h Also at State Key Laboratory of Nuclear Physics and Technology, Peking University, Beijing 100871, People's Republic of China

ⁱ Also at School of Physics and Electronics, Hunan University, Changsha 410082, China

^j Also at Guangdong Provincial Key Laboratory of Nuclear Science, Institute of Quantum Matter, South China Normal University, Guangzhou 510006, China

^k Also at Frontiers Science Center for Rare Isotopes, Lanzhou University, Lanzhou 730000, People's Republic of China

^l Also at Lanzhou Center for Theoretical Physics, Lanzhou University, Lanzhou 730000, People's Republic of China

^m Also at the Department of Mathematical Sciences, IBA, Karachi , Pakistan

E-mail: besiii-publications@ihep.ac.cn

ABSTRACT: The Born cross sections of the $e^+e^- \rightarrow D^{*+}D^{*-}$ and $e^+e^- \rightarrow D^{*+}D^-$ processes are measured using e^+e^- collision data collected with the BESIII experiment at center-of-mass energies from 4.085 to 4.600 GeV, corresponding to an integrated luminosity of 15.7 fb^{-1} . The results are consistent with and more precise than the previous measurements by the Belle, Babar and CLEO collaborations. The measurements are essential for understanding the nature of vector charmonium and charmonium-like states.

KEYWORDS: Cross section, Charmonium states, Charmonium-like states, e^+e^- experiments

Contents

1	Introduction	1
2	BESIII detector and data samples	2
3	Event selection and background analysis	5
4	Signal yield determination	6
5	Cross section measurements	8
6	Systematic uncertainties	10
7	Summary	12

1 Introduction

The masses and decay patterns of conventional vector ($J^{PC} = 1^{--}$) charmonium states match well the predictions from the quark potential model [1]. They decay dominantly into open-charm final states when their masses are above the open-charm threshold, such as $\psi(4040)$ and $\psi(4160)$. However, puzzles come when numerous vector charmonium-like states not expected in the quark potential model, such as $Y(4260)$ [2–5] and $Y(4360)$ [6–8], have been observed. Later, more precise data indicates that the line shape of $Y(4260)$ is asymmetric and its mass is close to $4220 \text{ MeV}/c^2$ [9–11]. The measured masses of these charmonium-like states are above the open-charm threshold. In contrast to conventional states at the same energy region, they mainly decay into hidden-charm final states. However, the state around $4220 \text{ MeV}/c^2$ which was observed in open-charm production process $e^+e^- \rightarrow Y(4220) \rightarrow \pi^+ D^0 \bar{D}^{*-}$ in the BESIII experiment [12] is consistent with previous observations of the $Y(4220)$ state [9–11]. A closer examination of these states in open-charm channels may provide further insights on the nature of these states and offer necessary inputs to different theoretical interpretations including compact tetraquarks, molecules, hybrids, or hadrocharmonia [13–19].

The previously measured cross sections of $e^+e^- \rightarrow D^{*+}D^{*-}$ and $e^+e^- \rightarrow D^{*+}D^-$ at energy points from 3.875 to 6 GeV [20–23] have been used to understand the vector charmonium(-like) states. Authors of Ref. [24] found that the cross sections of the $e^+e^- \rightarrow D^{*+}D^{*-}$ process can be described well by the conventional charmonium states $\psi(4040)$, $\psi(4160)$, $\psi(4415)$, and a $\bar{D}D_1(2420)$ hadronic molecule hypothesis of the $Y(4260)$. Authors of Ref. [25] used a coupled-channel approach to perform a simultaneous fit to the data in the open-charm channels including $e^+e^- \rightarrow D^{*+}D^{*-}$ and $e^+e^- \rightarrow D^{*+}D^-$. The fit provides a remarkably good overall description of all the line shapes, with five vector charmonium

resonances, $\psi(2S)$, $\psi(3770)$, $\psi(4040)$, $\psi(4160)$, and $\psi(4415)$. Recently, extensive numerical analyses were performed in Ref. [26] by combining all the cross sections of the final states $J/\psi\pi^+\pi^-$, $h_c\pi^+\pi^-$, $D^0D^{*-}\pi^+$, $\psi(2S)\pi^+\pi^-$, $\omega\chi_{c0}$, and $J/\psi\eta$ measured in the BESIII, Belle, and BaBar experiments, together with those of the open-charm final states $D^{*+}D^{*-}$ and $D^{*+}D^-$ measured by Belle (with and without $D_s^{*+}D_s^{*-}$ channel). It is concluded that the $Y(4260)$ may be interpreted as a mixture of 4^3S_1 and $3^3D_1(2^3D_1)$ charmonium states. However, more precise measurements are necessary to verify these conclusions.

In this article, we present improved measurements of the Born cross sections of the $e^+e^- \rightarrow D^{*+}D^{*-}$ and $e^+e^- \rightarrow D^{*+}D^-$ processes at 28 center-of-mass (c.m.) energies (\sqrt{s}) from 4.085 to 4.600 GeV.

2 BESIII detector and data samples

The data were collected by the BESIII detector [27], and the total integrated luminosity is 15.7 fb^{-1} . The c.m. energies were measured using $e^+e^- \rightarrow \mu^+\mu^-$ events with an uncertainty of 0.8 MeV [28] and the integrated luminosities were measured using Bhabha scattering events to an uncertainty of 1.0% [29, 30]. The data samples used in this analysis and the corresponding integrated luminosities are listed in Tables 1 and 2.

The BESIII detector [27] records symmetric e^+e^- collisions provided by the BEPCII storage ring [31], which operates with a peak luminosity of $1 \times 10^{33} \text{ cm}^{-2}\text{s}^{-1}$ in the c.m. energy range from 2.0 to 4.95 GeV [32]. The cylindrical core of the BESIII detector covers 93% of the full solid angle and consists of a helium-based multilayer drift chamber (MDC), a plastic scintillator time-of-flight system (TOF), and a CsI(Tl) electromagnetic calorimeter (EMC), which are all enclosed in a superconducting solenoidal magnet providing a 1.0 T magnetic field. The solenoid is supported by an octagonal flux-return yoke with resistive plate counter muon identification modules interleaved with steel. The charged-particle momentum resolution at 1 GeV/c is 0.5%, and the dE/dx resolution is 6% for electrons from Bhabha scattering. The EMC measures photon energies with a resolution of 2.5% (5%) at 1 GeV in the barrel (end cap) region. The time resolution in the TOF barrel region is 68 ps, while that in the end cap region is 110 ps. The end cap TOF system was upgraded in 2015 using multi-gap resistive plate chamber technology, providing a time resolution of 60 ps [33–35].

Simulated data samples produced with a GEANT4-based [36] Monte Carlo (MC) package, which includes the geometric description of the BESIII detector and the detector response, are used to determine detection efficiencies and to estimate background contributions. The simulation models, including the beam energy spread, initial state radiation (ISR), and vacuum polarization in the e^+e^- annihilations are treated with the generator KKMC [37, 38].

The signal MC samples of the $e^+e^- \rightarrow D^{*+}D^{*-}$ and $e^+e^- \rightarrow D^{*+}D^-$ processes with 100,000 events are generated using phase-space (PHSP) [39, 40] and helicity-amplitude (HELAMP) [39, 40] models at each c.m. energy, respectively. These signal models describe data well at each energy point. The D^{*+} meson is reconstructed by using the decay chain $D^{*+} \rightarrow \pi^+D^0$, $D^0 \rightarrow K^-\pi^+$, while the D^{*-} or D^- is not reconstructed exclusively but is

\sqrt{s} (GeV)	\mathcal{L}_{int} (pb $^{-1}$)	$N_{D^{*+}}^{\text{sig}}$	$\epsilon_{D^{*+}}$	$(1 + \delta)_{D^{*+}} 1 - \Pi ^{-2}$	$\sigma_{D^{*+}}^{\text{B}}$ (pb)	$N_{D^{*-}}^{\text{sig}}$	$\epsilon_{D^{*-}}$	$(1 + \delta)_{D^{*-}} 1 - \Pi ^{-2}$	$\sigma_{D^{*-}}^{\text{B}}$ (pb)	σ_a^{B} (pb)
4.0854	52.9	188 \pm 15	0.055	0.845	2867 \pm 228 \pm 174	194 \pm 16	0.054	0.838	3009 \pm 241 \pm 144	2949 \pm 259
4.1285	393.4	2374 \pm 53	0.082	0.863	3205 \pm 72 \pm 168	2379 \pm 53	0.083	0.874	3121 \pm 70 \pm 159	3158 \pm 178
4.1574	406.9	3086 \pm 61	0.100	0.893	3177 \pm 63 \pm 164	2972 \pm 60	0.100	0.897	3052 \pm 61 \pm 154	3106 \pm 170
4.1780	3189.0	25370 \pm 171	0.120	0.935	2652 \pm 18 \pm 122	25697 \pm 171	0.120	0.932	2701 \pm 18 \pm 137	2662 \pm 126
4.1886	570.0	4358 \pm 72	0.121	0.946	2496 \pm 41 \pm 119	4276 \pm 71	0.122	0.958	2394 \pm 40 \pm 119	2448 \pm 126
4.1989	526.0	3608 \pm 65	0.125	1.000	2046 \pm 37 \pm 98	3651 \pm 66	0.126	0.987	2081 \pm 37 \pm 104	2061 \pm 107
4.2092	572.1	3318 \pm 64	0.128	1.057	1600 \pm 31 \pm 84	3440 \pm 65	0.128	1.037	1689 \pm 32 \pm 91	1638 \pm 92
4.2171	569.2	2653 \pm 59	0.127	1.208	1136 \pm 25 \pm 55	2710 \pm 59	0.124	1.228	1170 \pm 26 \pm 59	1150 \pm 62
4.2263	1100.9	4150 \pm 77	0.137	1.365	754 \pm 14 \pm 36	3890 \pm 74	0.136	1.463	665 \pm 13 \pm 32	696 \pm 36
4.2357	530.3	1233 \pm 48	0.128	2.105	323 \pm 12 \pm 19	1188 \pm 45	0.126	1.994	332 \pm 13 \pm 19	327 \pm 23
4.2438	538.1	1030 \pm 45	0.123	2.249	258 \pm 11 \pm 16	954 \pm 44	0.123	2.313	234 \pm 11 \pm 14	245 \pm 19
4.2580	828.4	1474 \pm 52	0.133	2.024	247 \pm 9 \pm 15	1561 \pm 57	0.135	2.026	258 \pm 9 \pm 15	252 \pm 17
4.2668	531.1	990 \pm 43	0.135	1.755	295 \pm 13 \pm 16	1032 \pm 43	0.134	1.703	318 \pm 13 \pm 16	308 \pm 20
4.2777	175.7	338 \pm 23	0.135	1.582	336 \pm 23 \pm 21	367 \pm 25	0.136	1.532	375 \pm 25 \pm 19	357 \pm 30
4.2879	491.5	1074 \pm 40	0.138	1.312	452 \pm 17 \pm 23	1079 \pm 40	0.137	1.314	455 \pm 17 \pm 24	454 \pm 29
4.3079	45.1	118 \pm 13	0.157	1.216	511 \pm 55 \pm 35	158 \pm 14	0.164	1.094	726 \pm 65 \pm 45	596 \pm 68
4.3121	492.1	1453 \pm 43	0.156	1.068	661 \pm 20 \pm 33	1496 \pm 44	0.155	1.135	645 \pm 19 \pm 30	651 \pm 37
4.3374	501.1	1998 \pm 49	0.169	1.034	854 \pm 21 \pm 43	1980 \pm 49	0.168	1.013	869 \pm 21 \pm 43	861 \pm 48
4.3583	543.9	2550 \pm 55	0.183	0.999	958 \pm 21 \pm 49	2555 \pm 55	0.186	1.008	937 \pm 20 \pm 44	945 \pm 50
4.3774	522.8	2403 \pm 53	0.181	1.007	946 \pm 21 \pm 49	2507 \pm 54	0.179	0.999	1001 \pm 21 \pm 51	973 \pm 54
4.3874	55.6	323 \pm 19	0.195	0.947	1180 \pm 70 \pm 63	259 \pm 18	0.190	1.058	868 \pm 59 \pm 43	969 \pm 76
4.3964	505.0	2462 \pm 53	0.185	1.030	959 \pm 21 \pm 46	2403 \pm 53	0.188	0.997	951 \pm 21 \pm 50	956 \pm 52
4.4156	1090.7	4963 \pm 76	0.193	1.044	845 \pm 13 \pm 40	4963 \pm 76	0.193	1.060	833 \pm 13 \pm 40	839 \pm 42
4.4362	568.1	2211 \pm 52	0.189	1.119	690 \pm 16 \pm 34	2397 \pm 54	0.192	1.082	759 \pm 17 \pm 36	721 \pm 39
4.4671	111.1	327 \pm 20	0.188	1.261	465 \pm 29 \pm 25	333 \pm 21	0.188	1.288	463 \pm 29 \pm 23	464 \pm 35
4.5271	112.1	280 \pm 19	0.191	1.246	394 \pm 27 \pm 22	302 \pm 20	0.198	1.192	428 \pm 28 \pm 24	410 \pm 34
4.5745	48.9	145 \pm 13	0.206	1.130	475 \pm 44 \pm 24	145 \pm 13	0.201	1.192	462 \pm 42 \pm 32	469 \pm 47
4.5995	586.9	1479 \pm 43	0.204	1.238	373 \pm 11 \pm 18	1473 \pm 43	0.202	1.219	381 \pm 11 \pm 18	377 \pm 21

Table 1. The Born cross section of $e^+e^- \rightarrow D^{*+}D^{*-}$, σ^{B} , together with the integrated luminosity \mathcal{L}_{int} , the number of signal events N^{sig} , the reconstruction efficiency ϵ , and the product of the ISR correction factor and vacuum polarization factor $(1 + \delta)|1 - \Pi|^{-2}$. The subscripts D^{*+} , D^{*-} , and a denote the results for the reconstructed D^{*+} candidates, reconstructed D^{*-} candidates, and the average values, respectively. The first uncertainties in $\sigma_{D^{*+}}^{\text{B}}$ and $\sigma_{D^{*-}}^{\text{B}}$ are statistical and the second systematic; the uncertainties in σ_a^{B} include the statistical and systematic uncertainties calculated using the same method as in Ref. [41].

\sqrt{s} (GeV)	\mathcal{L}_{int} (pb $^{-1}$)	$N_{D^{*+}}^{\text{sig}}$	$\epsilon_{D^{*+}}$	$(1 + \delta)_{D^{*+}} 1 - \Pi ^{-2}$	$\sigma_{D^{*+}}^{\text{B}}$ (pb)	$N_{D^{*-}}^{\text{sig}}$	$\epsilon_{D^{*-}}$	$(1 + \delta)_{D^{*-}} 1 - \Pi ^{-2}$	$\sigma_{D^{*-}}^{\text{B}}$ (pb)	σ_c^{B} (pb)
4.0854	52.9	178 \pm 14	0.135	0.975	947 \pm 76 \pm 55	162 \pm 13	0.131	1.027	850 \pm 70 \pm 48	1785 \pm 84
4.1285	393.4	1028 \pm 34	0.141	1.110	627 \pm 21 \pm 31	1068 \pm 35	0.141	1.055	681 \pm 22 \pm 33	1303 \pm 38
4.1574	406.9	1070 \pm 35	0.160	1.065	581 \pm 19 \pm 32	1137 \pm 36	0.156	1.057	632 \pm 20 \pm 31	1217 \pm 37
4.1780	3189.0	8634 \pm 101	0.173	1.094	536 \pm 6 \pm 27	8472 \pm 100	0.173	1.107	518 \pm 6 \pm 26	1052 \pm 27
4.1886	570.0	1377 \pm 40	0.171	1.148	460 \pm 14 \pm 22	1423 \pm 41	0.171	1.117	489 \pm 14 \pm 24	947 \pm 26
4.1989	526.0	1292 \pm 39	0.178	1.124	462 \pm 14 \pm 24	1278 \pm 39	0.175	1.125	460 \pm 14 \pm 22	923 \pm 26
4.2092	572.1	1280 \pm 39	0.178	1.180	400 \pm 12 \pm 20	1278 \pm 39	0.175	1.168	409 \pm 12 \pm 20	808 \pm 23
4.2171	569.2	1251 \pm 39	0.180	1.184	389 \pm 12 \pm 19	1270 \pm 38	0.179	1.184	393 \pm 12 \pm 19	781 \pm 22
4.2263	1100.9	2456 \pm 54	0.194	1.212	356 \pm 8 \pm 17	2350 \pm 53	0.192	1.248	331 \pm 8 \pm 16	684 \pm 18
4.2357	530.3	1217 \pm 38	0.194	1.142	385 \pm 12 \pm 19	1136 \pm 37	0.192	1.177	356 \pm 11 \pm 17	738 \pm 21
4.2438	538.1	1157 \pm 37	0.196	1.172	351 \pm 11 \pm 17	1188 \pm 37	0.195	1.154	367 \pm 12 \pm 18	715 \pm 21
4.2580	828.4	2007 \pm 49	0.208	1.131	385 \pm 9 \pm 19	1872 \pm 47	0.207	1.149	356 \pm 9 \pm 18	738 \pm 20
4.2668	531.1	1301 \pm 39	0.208	1.108	397 \pm 12 \pm 19	1286 \pm 39	0.207	1.100	396 \pm 12 \pm 20	793 \pm 22
4.2777	175.7	422 \pm 22	0.205	1.121	390 \pm 21 \pm 19	468 \pm 23	0.209	1.033	464 \pm 23 \pm 24	835 \pm 29
4.2879	491.5	1161 \pm 37	0.204	1.112	391 \pm 13 \pm 19	1166 \pm 37	0.203	1.128	387 \pm 12 \pm 19	778 \pm 22
4.3079	45.1	109 \pm 11	0.224	1.131	355 \pm 37 \pm 19	101 \pm 11	0.224	1.141	333 \pm 35 \pm 20	688 \pm 37
4.3121	492.1	1079 \pm 36	0.211	1.191	327 \pm 11 \pm 16	1142 \pm 37	0.212	1.089	376 \pm 12 \pm 18	694 \pm 20
4.3374	501.1	1182 \pm 37	0.223	1.091	360 \pm 11 \pm 17	1150 \pm 37	0.224	1.131	339 \pm 11 \pm 17	699 \pm 20
4.3583	543.9	1342 \pm 40	0.242	1.112	343 \pm 10 \pm 16	1320 \pm 39	0.236	1.124	342 \pm 10 \pm 17	685 \pm 19
4.3774	522.8	1259 \pm 38	0.233	1.101	351 \pm 11 \pm 17	1215 \pm 38	0.231	1.102	342 \pm 11 \pm 16	692 \pm 19
4.3874	55.6	136 \pm 12	0.246	1.131	332 \pm 30 \pm 16	146 \pm 13	0.248	1.068	371 \pm 34 \pm 19	695 \pm 32
4.3964	505.0	1191 \pm 38	0.238	1.107	334 \pm 11 \pm 16	1277 \pm 38	0.240	1.064	370 \pm 11 \pm 19	693 \pm 20
4.4156	1090.7	2688 \pm 56	0.245	1.094	344 \pm 7 \pm 16	2672 \pm 56	0.246	1.113	334 \pm 7 \pm 16	677 \pm 17
4.4362	568.1	1444 \pm 41	0.250	1.073	355 \pm 10 \pm 17	1387 \pm 40	0.248	1.096	337 \pm 10 \pm 16	690 \pm 19
4.4671	111.1	282 \pm 18	0.253	1.083	345 \pm 22 \pm 16	265 \pm 17	0.253	1.114	318 \pm 21 \pm 15	661 \pm 24
4.5271	112.1	260 \pm 17	0.261	1.144	290 \pm 19 \pm 14	257 \pm 17	0.265	1.116	288 \pm 19 \pm 14	579 \pm 22
4.5745	48.9	78 \pm 10	0.255	1.304	177 \pm 22 \pm 11	104 \pm 11	0.266	1.175	255 \pm 26 \pm 14	418 \pm 25
4.5995	586.9	1085 \pm 36	0.268	1.162	224 \pm 7 \pm 11	1146 \pm 37	0.269	1.185	229 \pm 7 \pm 12	451 \pm 13

Table 2. The Born cross sections of $e^+e^- \rightarrow D^{*+}D^-$ ($\sigma_{D^{*+}}^{\text{B}}$) and $e^+e^- \rightarrow D^{*-}D^+$ ($\sigma_{D^{*-}}^{\text{B}}$), together with the integrated luminosity \mathcal{L}_{int} , the number of signal events N^{sig} , the reconstruction efficiency ϵ , and the product of the ISR correction factor and vacuum polarization factor $(1 + \delta)|1 - \Pi|^{-2}$. The subscripts D^{*+} , D^{*-} , and c denote the results for the reconstructed D^{*+} candidates, reconstructed D^{*-} candidates, and the combined values, respectively. The first uncertainties in $\sigma_{D^{*+}}^{\text{B}}$ and $\sigma_{D^{*-}}^{\text{B}}$ are statistical and the second systematic; the uncertainties in σ_c^{B} include the statistical and systematic uncertainties calculated using the same method as in Ref. [41].

inferred from energy-momentum conservation. Inclusion of charge-conjugated (*c.c.*) states is implicit unless otherwise stated.

Generic MC samples spread over the complete energy range are used to analyze the possible background contributions. The generic MC sample includes the production of open-charm processes, the ISR production of vector charmonium(-like) states, and the continuum processes incorporated in KKMC [37, 38]. The known decay modes are modelled with EVTGEN [39, 40] using branching fractions taken from the Particle Data Group [42], and the remaining unknown charmonium decays are modelled with LUNDCHARM [43, 44]. Final-state radiation (FSR) from charged final-state particles is incorporated using PHOTOS [45].

In addition, exclusive MC samples with 100,000 events each for the processes $e^+e^- \rightarrow D^{*+}\bar{D}^0\pi^-$, $D^{*-}D^0\pi^+$, $D^{*+}\bar{D}^{*0}\pi^-$, $D^{*-}D^{*0}\pi^+$, $D^{*+}D^-\pi^0$, $D^0D^-\pi^+$, and $D^{*0}\bar{D}^{*0}$ (listed in Table 3) are generated with PHSP model at each c.m. energy to study possible background contributions. Similarly, only D^{*+} is reconstructed while others are inferred from energy-momentum conservation. Here $e^+e^- \rightarrow D^{*+}\bar{D}^0\pi^-$ and $D^{*-}D^0\pi^+$, and $e^+e^- \rightarrow D^{*+}\bar{D}^{*0}\pi^-$ and $D^{*0}D^{*-}\pi^+$ are two pairs of charge-conjugated modes, which have the same input line shapes of cross sections. The background contributions at all the energy points are found to be the same.

Exclusively generated MC samples			
$e^+e^- \rightarrow D^{*+}\bar{D}^0\pi^-$,	$D^{*+} \rightarrow \pi^+D^0$,	$D^0 \rightarrow K^-\pi^+$,	$\bar{D}^0 \rightarrow \text{anything}$
$e^+e^- \rightarrow D^{*-}D^0\pi^+$,	$D^0 \rightarrow K^-\pi^+$	$D^{*-} \rightarrow \text{anything}$	
$e^+e^- \rightarrow D^{*+}\bar{D}^{*0}\pi^-$,	$D^{*+} \rightarrow \pi^+D^0$	$D^0 \rightarrow K^-\pi^+$,	$\bar{D}^{*0} \rightarrow \text{anything}$
$e^+e^- \rightarrow D^{*-}D^{*0}\pi^+$,	$D^{*0} \rightarrow \pi^0D^0(\gamma D^0)$,	$D^0 \rightarrow K^-\pi^+$,	$D^{*-} \rightarrow \text{anything}$
$e^+e^- \rightarrow D^{*+}D^-\pi^0$,	$D^{*+} \rightarrow \pi^+D^0$	$D^0 \rightarrow K^-\pi^+$,	$D^- \rightarrow \text{anything}$
$e^+e^- \rightarrow D^-D^0\pi^+$,	$D^0 \rightarrow K^-\pi^+$,	$D^- \rightarrow \text{anything}$	
$e^+e^- \rightarrow D^{*0}\bar{D}^{*0}$,	$D^{*0} \rightarrow \text{anything}$,	$\bar{D}^{*0} \rightarrow \text{anything}$	

Table 3. The decay chains of the exclusively generated MC samples for background studies.

3 Event selection and background analysis

Candidate events with at least two pions with positive charge and at least one kaon with negative charge are selected. The charged tracks are required to be well reconstructed in the MDC with a polar angle θ satisfying $|\cos\theta| < 0.93$, and the distances of the closest approach to the interaction point in $x - y$ plane and z direction of e^+e^- c.m. frame have to be less than 1 cm and 10 cm, respectively. The particle identification (PID) of kaons and pions is based on the dE/dx and time of flight information. Assumption of a given particle identification is based on the larger of the two PID-hypothesis probabilities $P(h)$, $h = K, \pi$. Kaon candidates are required to satisfy $P(K) > P(\pi)$ and $P(K) > 0.001$ with momenta larger than 0.3 GeV/*c*. Pion candidates are required to satisfy $P(\pi) > P(K)$ and $P(\pi) > 0.001$. The pions with momenta less than 0.3 GeV/*c* are named as π_L^+ , whereas the

ones with momenta larger than $0.3 \text{ GeV}/c$ are named as π_H^+ . At least one π_L^+ and one π_H^+ are required in the final states.

We assume each input charged track originated from a common vertex, and a kinematic fit is performed to the $K^-\pi_H^+$ candidates, which constrains the masses of the $K^-\pi_H^+$ candidates to the known mass of the D^0 meson [42], to improve the track momentum resolution and to reduce background events. If there are multiple candidates in one event, we choose the $K^-\pi_H^+\pi_L^+$ combination with the smallest vertex and kinematic fit χ^2 and require $\chi^2 < 200$ for further studies. To identify signal candidates that involve the D^0 meson, we select events with a $K^-\pi_H^+$ invariant mass before the kinematic fit within a window of three standard deviations ($\pm 3\sigma$) around the D^0 known mass, $1845.4 < M(K^-\pi_H^+) < 1885.2 \text{ MeV}/c^2$, referred to as the D^0 mass window. Here σ is the measured mass resolution of D^0 meson. For the sake of simplicity, we use π^+ to replace π_L^+ in the following text.

After imposing all the requirements mentioned above, we use the two-dimensional (2D) distributions of the π^+D^0 invariant mass $M(\pi^+D^0)$ and recoil mass $RM(\pi^+D^0)$ after the kinematic fit, to study the signal and background contributions. Figure 1 shows the distributions of $RM(\pi^+D^0)$ versus $M(\pi^+D^0)$ for data, signal MC samples of $e^+e^- \rightarrow D^{*+}D^{*-}$ and $D^{*+}D^-$, and background MC samples of $e^+e^- \rightarrow D^{*+}\bar{D}^0\pi^-$, $D^{*-}D^0\pi^+$, $D^{*+}\bar{D}^{*0}\pi^-$, $D^{*0}D^{*-}\pi^+$, $D^{*+}D^-\pi^0$, $D^0D^-\pi^+$, and $e^+e^- \rightarrow D^{*0}\bar{D}^{*0}$ at 4.416 GeV , respectively.

The remaining background contributions are shown in Figure 2 together with the fit results where an Argus function [46] and a second-order Chebyshev polynomial are used to fit the $M(\pi^+D^0)$ and $RM(\pi^+D^0)$ distributions, respectively.

4 Signal yield determination

Two-dimensional unbinned fits to the recoil mass $RM(\pi^+D^0)$ versus the invariant mass $M(\pi^+D^0)$ distributions are performed to determine the signal yields of the $e^+e^- \rightarrow D^{*+}D^{*-}$ and $D^{*+}D^-$ processes. A 2D probability density function (PDF) $f(M, RM)$ is used to describe the data, where

$$\begin{aligned} f(M, RM) = & N^{\text{sig}1} s_1(M, RM) + N^{\text{sig}2} s_2(M, RM) \\ & + N^{\text{bkg}1} \left[\frac{R_1}{1+R_1} b_1(M, RM) + \frac{1}{1+R_1} b_2(M, RM) \right] \\ & + N^{\text{bkg}2} \left[\frac{R_2}{1+R_2} b_3(M, RM) + \frac{1}{1+R_2} b_4(M, RM) \right] \\ & + N^{\text{bkg}3} b_5(M, RM) + N^{\text{bkg}4} b_6(M, RM) \\ & + N^{\text{bkg}5} b_7(M, RM) + N^{\text{bkg}6} b_8(M, RM). \end{aligned} \quad (4.1)$$

Here, $s_1(M, RM)$ and $s_2(M, RM)$ are the signal PDFs for the $e^+e^- \rightarrow D^{*+}D^{*-}$ and $D^{*+}D^-$ processes, respectively, and are modeled using the signal MC shapes convoluted with corresponding Gaussian functions. The parameters of the Gaussian functions reflect the differences in the mass resolution between MC simulation and data, and are obtained from one-dimensional (1D) fits to the $M(\pi^+D^0)$ and $RM(\pi^+D^0)$ distributions. The $b_1(M, RM)$, $b_2(M, RM)$, $b_3(M, RM)$, $b_4(M, RM)$, $b_5(M, RM)$, $b_6(M, RM)$, and $b_7(M, RM)$ are the PDFs of the background processes $e^+e^- \rightarrow D^{*+}\bar{D}^0\pi^-$, $D^{*-}D^0\pi^+$, $D^{*+}\bar{D}^{*0}\pi^-$, $D^{*0}D^{*-}\pi^+$, $D^{*+}D^-\pi^0$, $D^0D^-\pi^+$, and $e^+e^- \rightarrow D^{*0}\bar{D}^{*0}$.

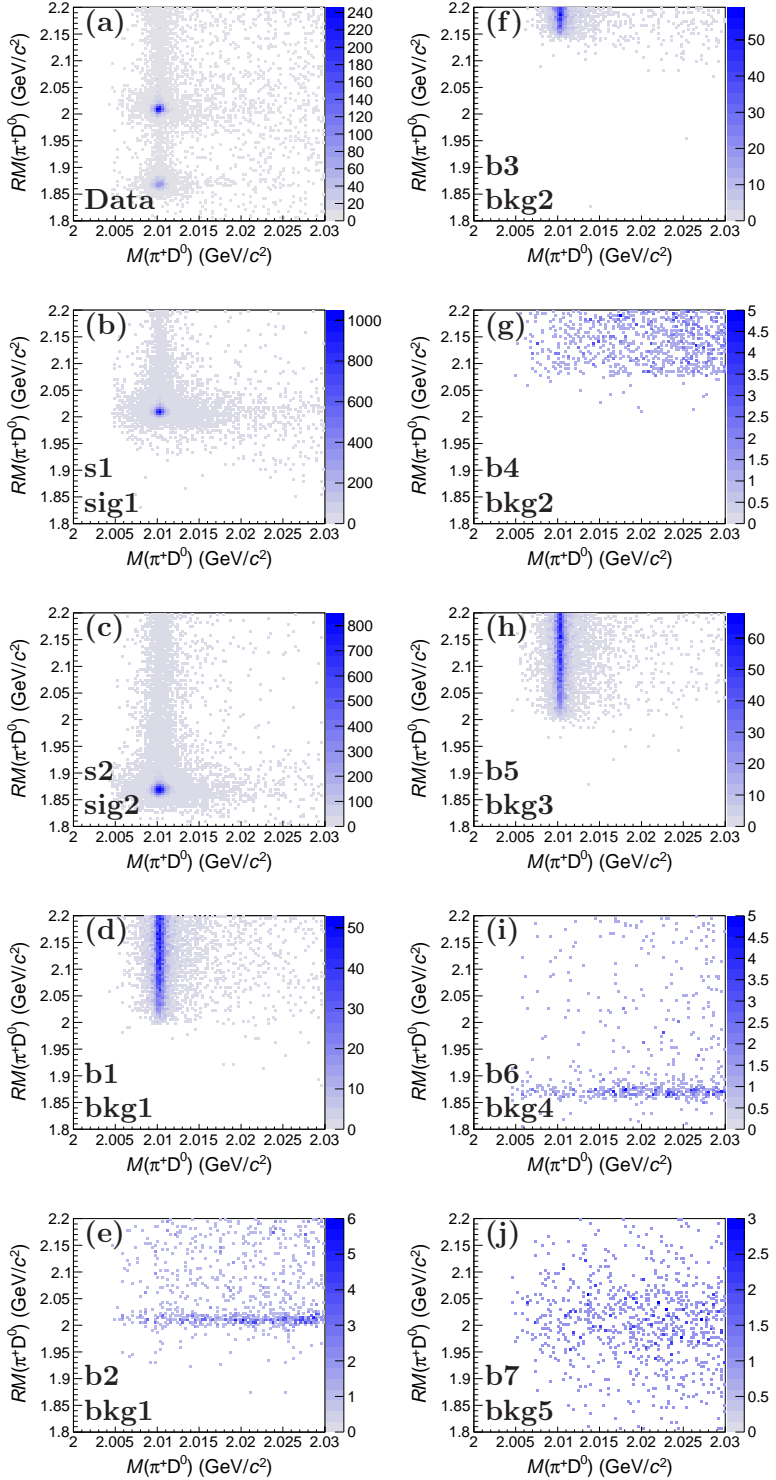


Figure 1. Distributions of the recoil mass $RM(\pi^+D^0)$ versus the invariant mass $M(\pi^+D^0)$ for (a) data, and the MC-simulated processes (b) $e^+e^- \rightarrow D^{*+}D^{*-}$, (c) $D^{*+}D^-$, (d) $D^{*+}\bar{D}^0\pi^-$, (e) $D^{*-}D^0\pi^+$, (f) $D^{*+}\bar{D}^{*0}\pi^-$, (g) $D^{*-}D^{*0}\pi^+$, (h) $D^{*+}D^-\pi^0$, (i) $D^-D^0\pi^+$, and (j) $D^{*0}\bar{D}^{*0}$ at 4.416 GeV c.m. energy, where plots (b) and (c) are the signal processes, and plots (d-j) are the background processes in this analysis. Labels of s1, sig1, b1, bkg1 etc. are used in eq.(4.1) and described in text.

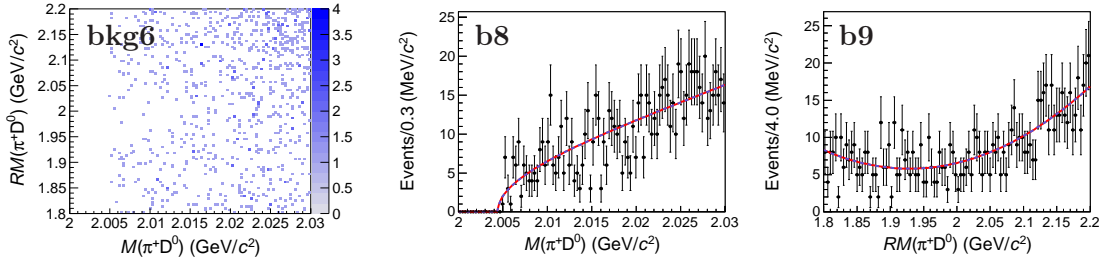


Figure 2. Distribution of the recoil mass $RM(\pi^+D^0)$ versus the invariant mass $M(\pi^+D^0)$ and the 2D fit result for the remaining background contributions of the generic MC samples after removing signal events and peaking background contributions mentioned in the text at 4.416 GeV c.m. energy. An Argus function and a second-order Chebyshev polynomial (red lines) are used to fit the $M(\pi^+D^0)$ and $RM(\pi^+D^0)$ distributions, respectively. Labels of bkg6, b8, and b9 are used in eq.(4.1) and described in text.

$D^{*-}D^{*0}\pi^+$, $D^{*+}D^-\pi^0$, $D^-D^0\pi^+$, and $D^{*0}\bar{D}^{*0}$ and are shown in Figure 1(d-j). The $b_8(M)$ and $b_9(RM)$ are the Argus function and second-order Chebyshev polynomial mentioned before. The PDFs for different contributions in eq.(4.1) vary for different c.m. energies.

The numbers of the signal events of $e^+e^- \rightarrow D^{*+}D^{*-}$ and $D^{*+}D^-$, the background events of $e^+e^- \rightarrow D^{*+}D^-\pi^0$, $D^-D^0\pi^+$, and $D^{*0}\bar{D}^{*0}$, and the flat background events are represented by $N_{\text{sig}1}$, $N_{\text{sig}2}$, $N_{\text{bkg}3}$, $N_{\text{bkg}4}$, $N_{\text{bkg}5}$ and $N_{\text{bkg}6}$, respectively; $N_{\text{bkg}1}$ is the total number of $e^+e^- \rightarrow D^{*+}\bar{D}^0\pi^-$ and $D^{*-}D^0\pi^+$, and $N_{\text{bkg}2}$ the total number of $e^+e^- \rightarrow D^{*+}\bar{D}^{*0}\pi^-$ and $D^{*-}D^{*0}\pi^+$. The ratios between the charge-conjugated modes of $e^+e^- \rightarrow D^{*+}\bar{D}^0\pi^-$ and $D^{*-}D^0\pi^+$, and $e^+e^- \rightarrow D^{*+}\bar{D}^{*0}\pi^-$ and $D^{*0}D^{*-}\pi^+$ are denoted by R_1 and R_2 , according to $R_1 = \mathcal{B}_{\text{bkg}1}\epsilon_{\text{bkg}1}/\mathcal{B}_{\text{bkg}1}^{c.c.}\epsilon_{\text{bkg}1}^{c.c.}$ and $R_2 = \mathcal{B}_{\text{bkg}2}\epsilon_{\text{bkg}2}/\mathcal{B}_{\text{bkg}2}^{c.c.}\epsilon_{\text{bkg}2}^{c.c.}$, where $\mathcal{B}_{\text{bkg}1}$, $\mathcal{B}_{\text{bkg}1}^{c.c.}$, $\mathcal{B}_{\text{bkg}2}$, and $\mathcal{B}_{\text{bkg}2}^{c.c.}$ are the products of branching fractions from the intermediate states for the processes $e^+e^- \rightarrow D^{*+}\bar{D}^0\pi^-$, $D^{*-}D^0\pi^+$, $D^{*+}\bar{D}^{*0}\pi^-$, and $D^{*0}D^{*-}\pi^+$, respectively. The corresponding reconstruction efficiencies are $\epsilon_{\text{bkg}1}$, $\epsilon_{\text{bkg}1}^{c.c.}$, $\epsilon_{\text{bkg}2}$, and $\epsilon_{\text{bkg}2}^{c.c.}$. All the numbers of events in the 2D fit are left free. The cross feeds from the charge-conjugated modes of signal channels are below 0.02% and therefore are neglected.

The 1D projections of the fit results to the $RM(\pi^+D^0)$ versus $M(\pi^+D^0)$ distributions at 4.416 GeV and the corresponding log-scale plots are shown in Figure 3. The distributions at other energy points are fitted using the same method to determine the signal yields, which are summarized in Tables 1 and 2.

5 Cross section measurements

The Born cross sections of the reaction channels $e^+e^- \rightarrow D^{*+}D^{*-}$ and $e^+e^- \rightarrow D^{*+}D^-$ are calculated with

$$\sigma^{\text{B}} = \frac{N^{\text{sig}}}{\mathcal{L}_{\text{int}}(1 + \delta)|1 - \Pi|^{-2}\mathcal{B}_1\mathcal{B}_2\epsilon}, \quad (5.1)$$

where N^{sig} is the signal yield; \mathcal{L}_{int} is the integrated luminosity; $|1 - \Pi|^{-2}$ is the vacuum polarization factor [47]; \mathcal{B}_1 and \mathcal{B}_2 are the branching fractions of $D^{*+} \rightarrow \pi^+D^0$ and $D^0 \rightarrow$

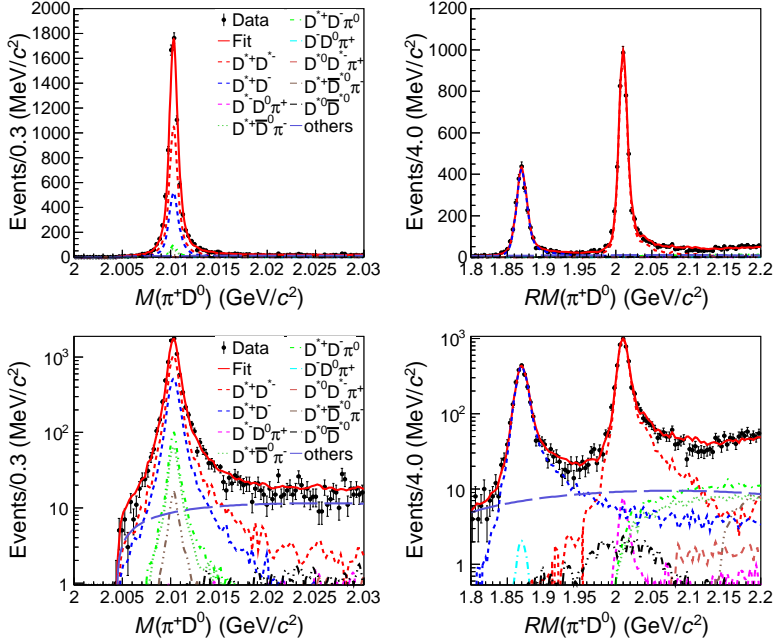


Figure 3. The 1D projections of the 2D fit (top) to the $RM(\pi^+ D^0)$ versus $M(\pi^+ D^0)$ distributions for the reconstructed D^{*+} candidates at 4.416 GeV and the corresponding log-scale plots (bottom). Dots with error bars are data. The red solid lines represent the fit result; the red and blue dashed lines denote the signal processes of $e^+e^- \rightarrow D^{*+}D^{*-}$ and $e^+e^- \rightarrow D^{*+}D^-$, respectively; the other dashed lines in different colors represent different background events.

$K^-\pi^+$ [42], respectively; ϵ is the reconstruction efficiency for the $e^+e^- \rightarrow D^{*+}D^{*-}$ or $e^+e^- \rightarrow D^{*+}D^-$ mode. The ISR correction factor $(1 + \delta)$ is obtained iteratively from the quantum electrodynamics calculation [37, 38, 48] by using the KKMC generator. The line shapes of Belle results [21] are used as a starting point to obtain the reconstruction efficiency and the ISR correction factor for each c.m. energy. Then the line shapes of the measured cross sections of $e^+e^- \rightarrow D^{*+}D^{*-}$ and $e^+e^- \rightarrow D^{*+}D^-$ are taken as inputs to re-calculate the efficiency and the ISR correction factor. This procedure is repeated until the difference of $(1 + \delta)\epsilon$ between two subsequent iterations is less than 3%. The Born cross sections of $e^+e^- \rightarrow D^{*+}D^{*-}$ and $e^+e^- \rightarrow D^{*+}D^-$, and the numbers used in the calculation are listed in Tables 1 and 2.

The cross sections of $e^+e^- \rightarrow D^{*+}D^{*-}$ for different c.m. energy points are shown in Figure 4(a) for the reconstructed D^{*+} and D^{*-} events, respectively. They are in agreement with each other within uncertainties. The average cross sections are calculated using the same method as in Ref. [41], where correlations between two measurements are considered. Figure 4(b) shows the comparison of the average cross sections of $e^+e^- \rightarrow D^{*+}D^{*-}$ between this work and those of the Belle [21] experiment. The results are overall compatible.

The cross sections of $e^+e^- \rightarrow D^{*+}D^-$ and $e^+e^- \rightarrow D^+D^{*-}$ for different c.m. energy points are shown in Figure 5(a). Again, the two results are in good agreement. The cross sections of $e^+e^- \rightarrow D^{*+}D^-$ and $e^+e^- \rightarrow D^+D^{*-}$ are averaged using the same method as

described above. The total cross sections of $e^+e^- \rightarrow D^{*+}D^- + c.c.$ are twice the average values. The comparison of the cross section of $e^+e^- \rightarrow D^{*+}D^- + c.c.$ between this work and those of the Belle [21] experiment is shown in Figure 5(b). They are overall compatible.

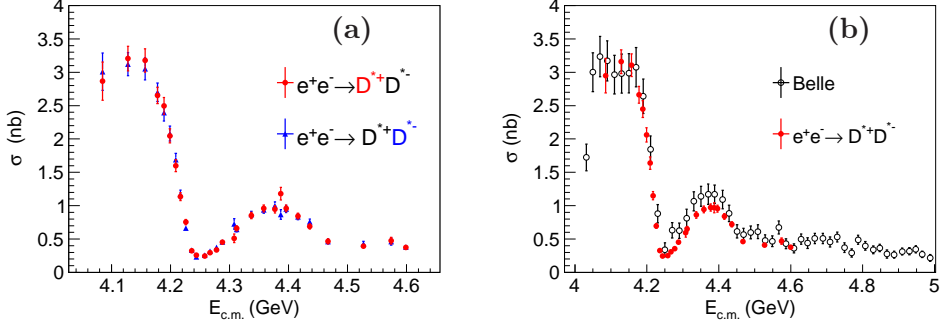


Figure 4. (a) The Born cross sections of $e^+e^- \rightarrow D^{*+}D^{*-}$ as a function of the c.m. energy for the reconstructed D^{*+} (red dots) and D^{*-} candidates (blue triangles). (b) The comparison of the average cross sections for $e^+e^- \rightarrow D^{*+}D^{*-}$ between this work (red dots) and those of the Belle experiment [21] (black circles). Error bars are the quadratic sum of statistical and systematic uncertainties.

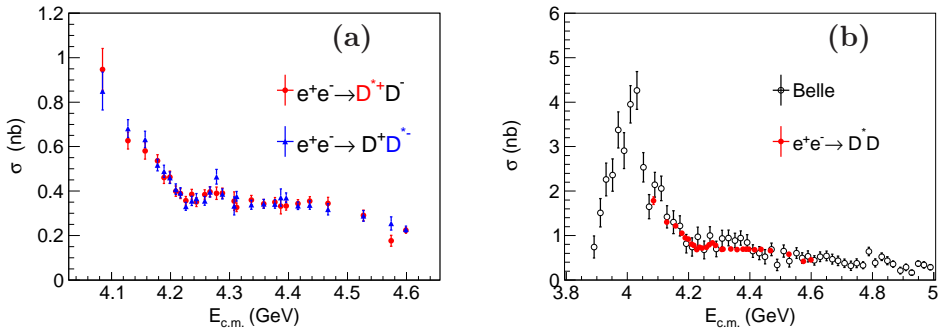


Figure 5. (a) The Born cross sections of the reaction channel $e^+e^- \rightarrow D^{*+}D^-$ for the reconstructed D^{*+} candidates (red dots) and $e^+e^- \rightarrow D^+D^-$ for the reconstructed D^{*-} candidates (blue triangles) as functions of the c.m. energy. (b) The comparison of the combined cross sections for $e^+e^- \rightarrow D^{*+}D^- + c.c.$ between this work (red dots) and those of the Belle experiment [21] (black circles). Error bars are the quadratic sum of statistical and systematic uncertainties.

6 Systematic uncertainties

The systematic uncertainties in the cross-section measurements mainly come from luminosity determination, track reconstruction efficiency, PID efficiency, and the branching fractions of the charmed meson decays, kinematic fit, ISR correction factor, fit range and modeling of the signal and background shapes. The uncertainty from the vacuum polarization is

negligible. The uncertainties due to luminosity, track reconstruction efficiency, PID efficiency, and the branching fractions of charmed meson decays are common while the other uncertainties are individual and uncommon for reconstructed D^{*+} and D^{*-} candidates.

- *Luminosity, track reconstruction efficiency, and PID efficiency.* The integrated luminosity is measured using Bhabha scattering events with an uncertainty of 1.0% [29, 30]. The uncertainty of the track reconstruction efficiency is 1.0% per track, taken from Ref. [12]. The uncertainty associated with PID efficiency is taken conservatively to be 1.0% per track [12].
- *Branching fractions.* The uncertainties of the branching fractions $\mathcal{B}(D^{*+} \rightarrow \pi^+ D^0)$ and $\mathcal{B}(D^0 \rightarrow K^- \pi^+)$ are 0.74% and 0.78% [42], respectively.

Therefore, the common systematic uncertainty is 4.49% in this analysis by summing the individual ones in quadrature.

- *Kinematic fit.* The systematic uncertainty from the kinematic fit is estimated by correcting the helix parameters of charged tracks according to the method described in Ref. [49]. The signal MC sample with the track helix parameter correction applied is taken as the nominal one. The difference between detection efficiencies obtained from MC samples with and without correction is taken as the systematic uncertainty. It is in the range between 0.86% and 2.40% for different energy points.
- *ISR correction factor.* The line shape of the cross section affects the ISR correction factor and the reconstruction efficiency. There are three uncertainties involved in the ISR correction factor. Firstly, the differences of $(1+\delta)\epsilon$ between the last two iterations are taken as the systematic uncertainties and are in the range between 0.00% and 2.71% (ISRI). Secondly, the input cross section at each energy point is changed randomly by varying the central value within its uncertainty and the $(1+\delta)$ and the efficiency ϵ are recalculated. This process is performed for 1000 times, and a Gaussian function is used to fit the $(1+\delta)\epsilon$ distribution. The width of the Gaussian function represents the statistical uncertainty of input line shape and varies between 0.01% and 0.60% (ISR2). Lastly, an alternative smooth method of LOWESS [50] is used instead of TSpline3 [51] for the input cross section line shape, and the differences in $(1+\delta)\epsilon$ values, varying between 0.01% to 3.73% (ISR3), are taken as the systematic uncertainties.
- *Fit range.* The systematic uncertainty caused by the choice of the fit range is estimated by varying the upper and lower bounds of the fit range by ± 10 MeV/ c^2 . Toy MC samples are generated using the obtained PDFs and the corresponding 2D fits are performed in the new fit range. This process has been repeated for 2000 times. The differences between the input values and the means of the output values are taken as the systematic uncertainties which vary between 0.05% and 1.61%.

- *Background shape.* The uncertainty attributed to the background shape is estimated by changing the background shape in $\pi^+ D^0$ recoil mass spectrum from the second-order Chebyshev polynomial to a linear function. The uncertainties due to the Argus function and PDFs of the peaking background contributions are checked and are found to be negligible. The systematic uncertainties due to the background shape vary between 0.01% and 1.95%.
- *Signal Shape.* The parameters of the Gaussian function, i.e., mean and resolution, describe the differences between data and signal MC simulation. The systematic uncertainty is assigned by varying the mean and resolution by \pm the corresponding uncertainties when performing the 2D fit. The systematic uncertainties are in the ranges of 0.01% to 3.54% and 0.02% to 5.01%, respectively.

All the uncommon systematic uncertainties for the reconstructed D^{*+} and D^{*-} candidates are summarized in Tables 4 and 5, respectively. The total uncommon systematic uncertainties at each energy point are the sum of individual ones in quadrature.

7 Summary

A measurement of the cross sections of the $e^+e^- \rightarrow D^{*+}D^{*-}$ and $e^+e^- \rightarrow D^{*+}D^-$ processes is presented using 28 data samples corresponding to a total integrated luminosity of 15.7 fb^{-1} with c.m. energies between 4.085 and 4.600 GeV. The cross sections are consistent with and more precise than those of the Belle, BaBar, and CLEO experiments. The structures in the cross sections measured by the previous experiments are confirmed. In order to finally reveal the nature of the vector charmonium(-like) states in this energy region, measurements on other two-body open-charm modes such as $D\bar{D}$, $D_s^+D_s^-$, $D_s^+D_s^{*-} + c.c.$, $D_s^{*+}D_s^{*-}$ [52] and multi-body modes such as $\pi D\bar{D}$, $\pi D^*\bar{D} + c.c.$, $\pi\pi D\bar{D}$ are necessary. More sophisticated models with further studies on coupled-channel effect are also needed.

Acknowledgments

The BESIII collaboration thanks the staff of BEPCII and the IHEP computing center for their strong support. This work is supported in part by National Key R&D Program of China under Contracts Nos. 2020YFA0406300, 2020YFA0406400; National Natural Science Foundation of China (NSFC) under Contracts Nos. 11625523, 11635010, 11735014, 11822506, 11835012, 11935015, 11935016, 11935018, 11961141012, 12022510, 12025502, 12035009, 12035013, 12061131003; the Chinese Academy of Sciences (CAS) Large-Scale Scientific Facility Program; Joint Large-Scale Scientific Facility Funds of the NSFC and CAS under Contracts Nos. U1732263, U1832207; CAS Key Research Program of Frontier Sciences under Contract No. QYZDJ-SSW-SLH040; 100 Talents Program of CAS; INPAC and Shanghai Key Laboratory for Particle Physics and Cosmology; ERC under Contract No. 758462; European Union Horizon 2020 research and innovation programme under Contract No. Marie Skłodowska-Curie grant agreement No 894790; German Research Foundation DFG under Contracts Nos. 443159800, Collaborative Research Center CRC 1044, FOR

\sqrt{s} (GeV)	Kinematic fit		ISR1		ISR2		ISR3		Fit range		Background shape		Mean		Resolution		T_{uncommon}	
	$D^{*+}D^{*-}$	$D^{*+}D^-$	$D^{*+}D^{*-}$	$D^{*+}D^-$	$D^{*+}D^{*-}$	$D^{*+}D^-$	$D^{*+}D^{*-}$	$D^{*+}D^-$	$D^{*+}D^{*-}$	$D^{*+}D^-$								
4.0854	2.10	2.15	0.35	1.31	0.03	0.13	0.41	0.39	0.72	0.37	0.04	0.17	1.83	1.54	2.82	2.04	4.07	3.63
4.1285	2.40	1.69	0.68	0.61	0.03	0.11	0.36	0.78	0.69	0.41	0.01	0.65	0.22	0.05	0.76	0.29	2.73	2.12
4.1574	1.96	2.07	1.10	2.13	0.01	0.07	0.80	0.02	0.88	0.24	0.03	0.42	0.17	0.48	0.24	0.66	2.56	3.12
4.1780	0.86	1.59	0.32	0.25	0.02	0.06	0.19	0.94	0.15	0.08	0.45	0.97	0.07	0.16	0.06	0.24	1.05	2.12
4.1886	1.40	1.61	0.68	0.49	0.03	0.12	0.46	0.13	0.28	0.56	0.11	0.22	0.01	0.20	0.08	0.03	1.65	1.81
4.1989	1.45	1.79	0.46	1.19	0.04	0.11	0.24	0.56	0.35	0.13	0.37	0.85	0.27	0.11	0.39	0.12	1.69	2.39
4.2092	2.40	1.55	1.21	1.09	0.05	0.14	0.41	0.08	0.41	0.34	0.22	0.47	0.31	0.45	0.15	0.32	2.78	2.07
4.2171	1.53	1.49	0.65	0.48	0.06	0.13	0.14	0.11	0.53	0.24	0.16	0.21	0.09	0.07	0.11	0.24	1.76	1.62
4.2263	1.50	1.79	0.39	0.27	0.09	0.12	0.12	0.25	0.48	0.26	0.10	0.11	0.32	0.07	0.25	0.13	1.68	1.86
4.2357	1.79	1.45	0.57	0.06	0.38	0.13	2.48	0.62	1.31	0.32	0.31	0.16	0.85	0.63	1.04	0.45	3.67	1.80
4.2438	1.99	1.43	1.94	0.22	0.52	0.16	2.18	0.22	1.03	0.37	0.39	0.24	2.31	0.23	0.21	0.61	4.07	1.65
4.2580	1.96	1.69	0.99	0.05	0.30	0.10	2.89	0.09	0.88	0.22	0.14	0.13	0.25	0.12	0.78	0.12	3.84	1.82
4.2668	2.03	1.34	1.01	0.57	0.34	0.13	0.51	0.27	1.61	0.40	0.29	0.37	0.85	0.17	1.67	0.17	3.29	1.53
4.2777	1.99	1.74	0.39	0.34	0.46	0.23	0.93	0.06	0.96	0.18	0.03	0.10	2.75	0.65	1.83	0.39	4.53	1.96
4.2879	1.82	1.39	1.91	0.38	0.15	0.14	0.09	0.29	1.45	0.61	0.25	0.17	0.46	0.34	0.33	0.94	2.46	1.86
4.3079	1.86	1.56	0.49	0.09	0.32	0.34	3.73	1.07	0.17	0.62	0.81	1.95	1.55	0.70	2.35	0.86	5.12	3.02
4.3121	1.83	1.48	0.41	0.05	0.17	0.32	0.61	0.32	0.52	0.39	0.62	0.60	0.17	0.26	0.06	0.91	2.15	1.95
4.3374	1.76	1.41	0.43	0.10	0.06	0.13	1.28	0.20	0.66	0.76	0.37	0.25	0.15	0.30	0.03	0.30	2.32	1.70
4.3583	1.68	1.39	0.21	0.06	0.04	0.12	0.62	0.03	0.27	0.51	0.27	0.23	0.24	0.09	0.39	0.23	2.47	1.71
4.3774	1.20	1.35	1.59	0.77	0.04	0.11	1.60	0.32	0.91	0.31	0.43	0.36	0.09	0.11	0.36	0.17	2.68	1.71
4.3874	1.22	1.44	1.43	0.85	0.15	0.54	1.43	0.12	0.31	0.38	0.31	0.52	0.31	0.08	0.32	0.11	2.84	1.72
4.3964	1.48	1.30	2.04	0.36	0.10	0.19	0.41	0.09	0.17	0.40	0.32	0.16	0.11	0.27	0.02	0.46	1.69	1.62
4.4156	1.26	1.30	0.59	0.66	0.05	0.09	0.77	0.03	0.10	0.17	0.12	0.11	0.06	0.16	0.04	0.18	1.53	1.36
4.4362	1.53	1.68	0.37	0.26	0.07	0.10	0.15	0.14	0.70	0.20	0.48	0.36	0.10	0.09	0.28	0.17	1.94	1.75
4.4671	1.71	1.46	0.77	0.14	0.27	0.21	1.01	0.14	0.30	0.08	0.32	0.08	0.31	0.39	1.94	0.35	2.97	1.58
4.5271	1.20	1.20	0.86	0.16	0.19	0.23	2.11	1.09	0.11	0.32	0.02	0.03	1.87	0.49	1.03	0.83	3.24	2.01
4.5745	1.30	1.32	0.18	0.56	0.17	0.60	0.93	2.27	0.11	0.97	0.57	0.59	1.08	3.54	0.92	0.30	2.31	4.66
4.5995	1.26	1.42	0.63	0.73	0.21	0.23	0.27	0.27	0.19	0.21	0.26	0.19	0.22	0.15	0.34	0.40	1.42	1.70

Table 4. The uncommon systematic uncertainties from kinematic fit, ISR correction factor, fit range, background shape, mean and resolution of signal shape for the reconstructed D^{*+} candidates (in units of %). The symbol T_{uncommon} is the total uncommon systematic uncertainty for the reconstructed D^{*+} candidates at each energy point obtained by summing individual ones in quadrature.

\sqrt{s} (GeV)	Kinematic fit		ISR1		ISR2		ISR3		Fit range		Background shape		Mean		Resolution		T_{uncommon}	
	$D^{*+}D^{*-}$	D^+D^{*-}	$D^{*+}D^{*-}$	D^+D^{*-}	$D^{*+}D^{*-}$	D^+D^{*-}	$D^{*+}D^{*-}$	D^+D^{*-}	$D^{*+}D^{*-}$	D^+D^{*-}								
4.0854	1.10	1.74	0.62	1.53	0.03	0.17	0.17	0.01	0.78	0.15	0.51	1.55	0.49	1.44	0.26	1.55	1.67	3.50
4.1285	2.19	1.73	0.95	0.35	0.03	0.10	0.13	0.30	0.25	0.15	0.09	0.61	0.27	0.29	0.05	0.39	2.43	1.96
4.1574	2.18	1.75	0.65	0.01	0.01	0.07	0.41	0.47	0.17	0.36	0.02	0.52	0.11	0.18	0.18	0.15	2.33	1.94
4.1780	1.19	1.71	1.91	0.88	0.02	0.06	0.37	0.01	0.55	0.15	0.41	0.87	0.04	0.11	0.08	0.04	2.38	2.12
4.1886	1.87	1.49	0.05	0.18	0.03	0.11	0.14	0.10	0.93	0.05	0.45	0.86	0.30	0.15	0.09	0.24	2.17	1.76
4.1989	2.04	1.17	0.31	0.35	0.04	0.11	0.25	0.27	0.72	0.35	0.21	0.45	0.12	0.38	0.35	0.12	2.24	1.44
4.2092	1.86	1.64	2.07	0.60	0.04	0.13	0.75	0.07	0.58	0.94	0.24	0.46	0.37	0.20	0.14	0.08	2.98	2.05
4.2171	1.31	1.93	1.44	0.29	0.06	0.13	0.46	0.22	0.91	0.48	0.15	0.22	0.19	0.05	0.55	0.31	2.27	2.06
4.2263	1.23	1.71	0.74	0.20	0.11	0.13	0.83	0.58	0.13	0.13	0.08	0.11	0.09	0.12	0.32	0.15	1.70	1.84
4.2357	2.16	1.82	2.08	0.12	0.36	0.14	1.64	0.06	1.06	0.22	0.08	0.04	0.72	0.22	0.36	0.15	3.69	1.87
4.2438	1.81	1.75	2.24	1.11	0.51	0.14	1.46	0.30	1.20	0.37	0.27	0.14	0.60	0.33	2.28	0.12	4.21	2.17
4.2580	1.92	1.69	2.71	1.15	0.33	0.11	1.02	0.53	0.84	0.18	0.13	0.15	0.49	0.11	0.23	0.16	3.63	2.14
4.2668	1.76	1.88	0.34	0.64	0.31	0.13	0.09	0.15	0.21	0.19	0.02	0.13	0.27	0.40	0.77	0.43	2.01	2.09
4.2777	1.88	1.70	0.12	1.06	0.35	0.18	0.22	1.19	0.89	0.14	0.38	0.22	1.16	0.69	0.88	0.18	2.60	2.46
4.2879	2.06	1.47	1.02	0.41	0.15	0.15	0.45	0.05	0.26	0.11	0.21	0.31	0.72	0.59	0.67	0.25	2.57	1.70
4.3079	1.88	1.80	0.72	0.00	0.18	0.36	2.92	2.76	0.21	0.52	0.34	0.14	2.40	1.30	0.10	1.69	4.30	3.98
4.3121	1.18	1.65	0.03	0.41	0.22	0.26	0.60	0.29	0.35	0.31	0.26	0.28	0.24	0.02	0.41	0.14	1.49	1.80
4.3374	1.90	1.58	0.12	1.49	0.06	0.15	0.67	0.77	0.28	0.44	0.19	0.10	0.17	0.35	0.30	0.35	2.07	2.41
4.3583	1.45	1.71	0.13	0.90	0.05	0.12	0.02	0.07	0.27	0.61	0.26	0.25	0.06	0.12	0.20	0.37	1.52	2.08
4.3774	1.53	1.26	1.05	0.03	0.04	0.11	1.06	0.40	0.76	0.38	0.47	0.48	0.19	0.30	0.15	0.27	2.33	1.52
4.3874	1.26	1.76	0.38	0.38	0.24	0.54	0.75	0.22	0.08	0.05	0.98	0.59	0.71	0.46	0.92	1.47	2.16	2.51
4.3964	1.78	1.62	1.86	1.63	0.08	0.18	0.51	0.26	0.26	0.49	0.25	0.23	0.24	0.21	0.28	0.22	2.67	2.40
4.4156	1.58	1.36	0.59	0.21	0.05	0.10	0.42	0.22	0.19	0.07	0.19	0.10	0.19	0.08	0.23	0.10	1.78	1.41
4.4362	1.07	1.64	1.02	0.34	0.06	0.11	0.35	0.02	0.18	0.37	0.28	0.19	0.13	0.02	0.32	0.13	1.60	1.74
4.4671	1.57	1.44	0.22	0.01	0.26	0.22	0.50	0.09	0.09	0.22	0.21	0.11	0.78	0.80	0.81	0.42	2.04	1.73
4.5271	1.48	1.52	0.17	1.07	0.16	0.21	2.15	0.03	0.11	0.46	0.13	0.14	1.19	0.86	1.39	0.09	3.20	2.12
4.5745	1.52	1.37	0.03	1.25	0.18	0.36	0.56	0.15	0.61	1.01	0.36	0.09	0.12	0.73	5.01	2.28	5.31	3.22
4.5995	1.34	1.60	0.22	1.64	0.18	0.26	0.12	0.01	0.16	0.08	0.35	0.09	0.44	0.02	0.73	0.38	1.66	2.33

Table 5. The uncommon systematic uncertainties from kinematic fit, ISR correction factor, fit range, background shape, mean and resolution of signal shape for the reconstructed D^{*-} candidates (in units of %). The symbol T_{uncommon} is the total uncommon systematic uncertainty for the reconstructed D^{*-} candidates at each energy point obtained by summing individual ones in quadrature.

2359, GRK 214; Istituto Nazionale di Fisica Nucleare, Italy; Ministry of Development of Turkey under Contract No. DPT2006K-120470; National Science and Technology fund; Olle Engkvist Foundation under Contract No. 200-0605; STFC (United Kingdom); The Knut and Alice Wallenberg Foundation (Sweden) under Contract No. 2016.0157; The Royal Society, UK under Contracts Nos. DH140054, DH160214; The Swedish Research Council; U. S. Department of Energy under Contracts Nos. DE-FG02-05ER41374, DE-SC-0012069.

References

- [1] T. Barnes, S. Godfrey, and E. S. Swanson, *Higher charmonia*, *Phys. Rev.* **D72** (2005) 054026.
- [2] BaBar Collaboration, *Observation of a broad structure in the $\pi^+\pi^-J/\psi$ mass spectrum around 4.26 GeV/c²*, *Phys. Rev. Lett.* **95** (2005) 142001.
- [3] BaBar Collaboration, *Study of the reaction $e^+e^- \rightarrow J/\psi\pi^+\pi^-$ via initial-state radiation at BaBar*, *Phys. Rev.* **D86** (2012) 051102(R).
- [4] Belle Collaboration, *Measurement of the $e^+e^- \rightarrow \pi^+\pi^-J/\psi$ cross section via initial-state radiation at Belle*, *Phys. Rev. Lett.* **99** (2007) 182004.
- [5] Belle Collaboration, *Study of $e^+e^- \rightarrow \pi^+\pi^-J/\psi$ and observation of a charged charmoniumlike state at Belle*, *Phys. Rev. Lett.* **110** (2013) 252002.
- [6] BaBar Collaboration, *Evidence of a broad structure at an invariant mass of 4.32 GeV/c² in the reaction $e^+e^- \rightarrow \pi^+\pi^-\psi(2S)$ measured at BaBar*, *Phys. Rev. Lett.* **98** (2007) 212001.
- [7] Belle Collaboration, *Observation of two resonant structures in $e^+e^- \rightarrow \pi^+\pi^-\psi(2S)$ via initial-state radiation at Belle*, *Phys. Rev. Lett.* **99** (2007) 142002.
- [8] BaBar Collaboration, *Study of the reaction $e^+e^- \rightarrow \psi(2S)\pi^+\pi^-$ via initial-state radiation at BaBar*, *Phys. Rev.* **D89** (2014) 111103(R).
- [9] BESIII Collaboration, *Precise measurement of the $e^+e^- \rightarrow \pi^+\pi^-J/\psi$ cross section at center-of-mass energies from 3.77 to 4.60 GeV*, *Phys. Rev. Lett.* **118** (2017) 092001.
- [10] BESIII Collaboration, *Evidence of two resonant structures in $e^+e^- \rightarrow \pi^+\pi^-h_c$* , *Phys. Rev. Lett.* **118** (2017) 092002.
- [11] BESIII Collaboration, *Cross section measurements of $e^+e^- \rightarrow \omega\chi_{c0}$ from $\sqrt{s} = 4.178$ to 4.278 GeV*, *Phys. Rev.* **D99** (2019) 091103(R).
- [12] BESIII Collaboration, *Evidence of a resonant structure in the $e^+e^- \rightarrow \pi^+D^0D^{*-}$ cross section between 4.05 and 4.60 GeV*, *Phys. Rev. Lett.* **122** (2019) 102002.
- [13] H. X. Chen, W. Chen, X. Liu, and S. L. Zhu, *The hidden-charm pentaquark and tetraquark states*, *Phys. Rep.* **639** (2016) 1.
- [14] A. Esposito, A. Pilloni and A. D. Polosa, *Multiquark resonances*, *Phys. Rep.* **668** (2017) 1.
- [15] R. F. Lebed, R. E. Mitchell, and E. S. Swanson, *Heavy-quark QCD exotica*, *Prog. Part. Nucl. Phys.* **93** (2017) 143.
- [16] A. Ali, J. S. Lange and S. Stone, *Exotics: Heavy pentaquarks and tetraquarks*, *Prog. Part. Nucl. Phys.* **97** (2017) 123.
- [17] S. L. Olsen, T. Skwarnicki, and D. Zieminska, *Nonstandard heavy mesons and baryons: Experimental evidence*, *Rev. Mod. Phys.* **90** (2018) 015003.

- [18] F. K. Guo, C. Hanhart, U. G. Meißner, Q. Wang, Q. Zhao, and B. S. Zou, *Hadronic molecules*, *Rev. Mod. Phys.* **90** (2018) 015004.
- [19] N. Brambilla, S. Eidelman, C. Hanhart, A. Nefediev, C. P. Shen, C. E. Thomas, A. Vairo, and C. Z. Yuan, *The XYZ states: Experimental and theoretical status and perspectives*, *Phys. Rep.* **873** (2020) 1.
- [20] Belle Collaboration, *Measurement of the near-threshold $e^+e^- \rightarrow D(*)\pm D^{(*)\mp}$ cross section using initial-state radiation*, *Phys. Lett.* **98** (2007) 092001.
- [21] Belle Collaboration, *Angular analysis of the $e^+e^- \rightarrow D(*)\pm D^{(*)\mp}$ process near the open charm threshold using initial-state radiation*, *Phys. Rev.* **D97** (2018) 012002(R).
- [22] BaBar Collaboration, *Exclusive initial-state-radiation production of the $D\bar{D}$, $D^*\bar{D}$, and $D^*\bar{D}^*$ systems*, *Phys. Rev.* **D79** (2009) 092001.
- [23] CLEO Collaboration, *Measurement of charm production cross sections in e^+e^- annihilation at energies between 3.97 and 4.26 GeV*, *Phys. Rev.* **D80** (2009) 072001.
- [24] S. R. Xue, H. J. Jing, F. K. Guo, and Q. Zhao, *Disentangling the role of the $Y(4260)$ in $e^+e^- \rightarrow D^*\bar{D}^*$ and $D_s^*\bar{D}_s^*$ via line shape studies*, *Phys. Lett.* **B779** (2018) 402.
- [25] T. V. Uglov, Y. S. Kalashnikova, A. V. Nefediev, G. V. Pakhlova, and P. N. Pakhlov, *Exclusive open-charm near-threshold cross sections in a coupled-channel approach*, *JETP Lett.* **105** (2017) 1.
- [26] Q. F. Cao, H. R. Qi, G. Y. Tang, Y. F. Xue, and H. Q. Zheng, *On leptonic width of $X(4260)$* , *Eur. Phys. J.* **C81** (2021) 83.
- [27] BESIII Collaboration, *Design and construction of the BESIII detector*, *Nucl. Instrum. Meth.* **A614** (2010) 345.
- [28] BESIII Collaboration, *Measurements of the center-of-mass energies at BESIII via the di-muon process*, *Chin. Phys.* **C40** (2016) 063001.
- [29] BESIII Collaboration, *Precision measurement of the integrated luminosity of the data taken by BESIII at center-of-mass energies between 3.810 GeV and 4.600 GeV*, *Chin. Phys.* **C39** (2015) 093001.
- [30] BESIII Collaboration, *Luminosity measurements for the R scan experiment at BESIII*, *Chin. Phys.* **C41** (2017) 063001.
- [31] C. H. Yu *et al.*, *BEPCII performance and beam dynamics studies on luminosity*, in *Proceedings of IPAC 2016*, Busan, Korea, 2016.
- [32] BESIII Collaboration, *Future physics programme of BESIII*, *Chin. Phys.* **C44** (2020) 040001.
- [33] X. Li *et al.*, *Study of MRPC technology for BESIII endcap-TOF upgrade*, *Rad. Det. Tech. Meth.* **1** (2017) 13.
- [34] Y. X. Guo *et al.*, *The study of time calibration for upgraded end cap TOF of BESIII*, *Rad. Det. Tech. Meth.* **1** (2017) 15.
- [35] P. Cao *et al.*, *Design and construction of the new BESIII endcap Time-of-Flight system with MRPC technology*, *Nucl. Instrum. Meth.* **A953** (2020) 163053.
- [36] GEANT4 Collaboration, *Geant4—a simulation toolkit*, *Nucl. Instrum. Meth.* **A506** (2003) 250.

- [37] S. Jadach, B. F. L. Ward, and Z. Was, *The precision Monte Carlo event generator KK for two-fermion final states in e^+e^- collisions*, *Comput. Phys. Commun.* **130** (2000) 260.
- [38] S. Jadach, B. F. L. Ward, and Z. Was, *Coherent exclusive exponentiation for precision Monte Carlo calculations*, *Phys. Rev. D* **63** (2001) 113009.
- [39] D. J. Lange, *The EvtGen particle decay simulation package*, *Nucl. Instrum. Meth. A* **462** (2001) 152.
- [40] R. G. Ping, *Event generators at BESIII*, *Chin. Phys. C* **32** (2008) 599.
- [41] G. D'Agostini, *On the use of the covariance matrix to fit correlated data*, *Nucl. Instrum. Meth. A* **346** (1994) 306.
- [42] Particle Data Group, *Review of particle physics*, *Prog. Theor. Exp. Phys.* **2020** (2020) 083C01.
- [43] J. C. Chen, G. S. Huang, X. R. Qi, D. H. Zhang, and Y. S. Zhu, *Event generator for J/ψ and $\psi(2S)$ decay*, *Phys. Rev. D* **62** (2000) 034003.
- [44] R. L. Yang, R. G. Ping, and H. Chen, *Tuning and validation of the Lundcharm model with J/ψ decays*, *Chin. Phys. Lett.* **31** (2014) 061301.
- [45] E. Richter-Was, *QED bremsstrahlung in semileptonic B and leptonic τ decays*, *Phys. Lett. B* **303** (1993) 163.
- [46] ARGUS Collaboration, *Search for Hadronic $b \rightarrow u$ Decays*, *Phys. Lett. B* **241** (1990) 278.
- [47] S. Actis *et al.* (Working group on radiative corrections and Monte Carlo generators for low energies), *Quest for precision in hadronic cross sections at low energy: Monte Carlo tools vs. experimental data*, *Eur. Phys. J. C* **66** (2010) 585.
- [48] E. A. Kuraev and V. S. Fadin, *Yad. Fiz.* **41** (1985) 733 [*Sov. J. Nucl. Phys.* **41** (1985) 466].
- [49] BESIII Collaboration, *Search for hadronic transition $\chi_{cJ} \rightarrow \eta_c \pi^+ \pi^-$ and observation of $\chi_{cJ} \rightarrow K\bar{K}\pi\pi\pi$* , *Phys. Rev. D* **87** (2013) 012002.
- [50] W. S. Cleveland, *Robust locally weighted regression and smoothing scatterplots*, *JASA* **74** (1979) 829.
- [51] C. H. Reinsch, *Smoothing by spline functions*, *Numer. Math.* **10** (1967) 177.
- [52] E. Eichten, K. Gottfried, T. Kinoshita, K. D. Lane, and T. M. Yan, *Charmonium: comparison with experiment*, *Phys. Rev. D* **21** (1980) 203.